ACS Photonics

pubs.acs.org/journal/apchd5 Article

Probing the Radiative Electromagnetic Local Density of States in Nanostructures with a Scanning Tunneling Microscope

Shuiyan Cao,[§] Mario Zapata-Herrera,[§] Alfredo Campos, Eric Le Moal, Sylvie Marguet, Gérald Dujardin, Mathieu Kociak, Javier Aizpurua, Andrei G. Borisov, and Elizabeth Boer-Duchemin*

Cite This: *ACS Photonics* 2020, 7, 1280–1289 Read Online

ACCESS | Metrics & More | Article Recommendations | Supporting Information

ABSTRACT: A novel technique for the investigation of the radiative contribution to the electromagnetic local density of states is presented. The inelastic tunneling current from a scanning tunneling microscope (STM) is used to locally and electrically excite the plasmonic modes of a triangular gold platelet. The radiative decay of these modes is detected through the transparent substrate in the far field. Emission spectra, which depend on the position of the STM excitation, as well as energy-filtered emission maps for particular spectral windows are acquired using this technique. The STM-nanosource spectroscopy and microscopy results are compared to those obtained from spatially resolved electron energy loss spectroscopy (EELS) maps on similar platelets. While EELS is known to be related to the total projected electromagnetic local density of states, the light emission from the STM-nanosource is shown here to select the radiative contribution. Full electromagnetic calculations are carried out to explain the experimental STM data and provide valuable insight into the radiative nature of the different contributions of the breathing and edge plasmon modes of the nanoparticles. Our results introduce the STM-nanosource as a tool to investigate and engineer light emission at the nanoscale.

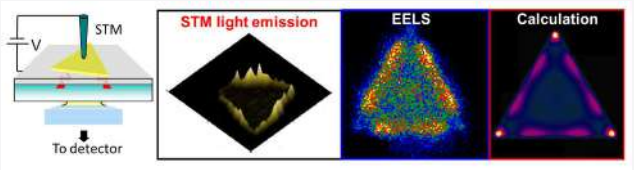

KEYWORDS: *electromagnetic local density of states, inelastic electron tunneling, electron energy loss spectroscopy, surface plasmon, scanning tunneling microscopy*

Increasing the rate or efficiency of elementary quantum processes in light sources is a current challenge. One way to do this is to engineer a fluorophore's emission properties by modifying its surrounding environment, thus influencing the electromagnetic local density of states (EM-LDOS).[1,2] Manipulating this quantity leads to, for example, improved quantum efficiencies for solar cells,[3] increased brightness for entangled photon pair emission,[4] or ultrafast sources based on spontaneous emission.[5] Thus, the measurement of the EM-LDOS is essential for the design and characterization of future nanophotonic devices and for further understanding of the role of the EM-LDOS in the emission of light.

The EM-LDOS is the number of electromagnetic modes at a particular energy existing at a particular point in space, where the contribution of each mode is determined by the intensity of the mode at that point.[2,6] Most often one considers the projected EM-LDOS, which takes into account the mode density only along a certain direction, i.e., that of the orientation of the dipole representing an emitter. The projected EM-LDOS at a given point in space determines the total decay rate Γ of a dipole emitter placed at that point, and it can be expressed using the dyadic Green's function.[2,7] Depending on the decay channels, the projected EM-LDOS may be further divided into the radiative (R-EM-LDOS) and nonradiative (NR-EM-LDOS) electromagnetic density of states, each associated, respectively, with the radiative and nonradiative partial decay rate contributions to Γ.[2] For an emitter placed in the vicinity of a plasmonic nanoparticle, the "bright" plasmon modes of the nano-object are those which are strongly coupled to the radiation continuum in the far field, thus providing a leading contribution to the R-EM-LDOS. The "dark" modes of the system, on the other hand, mainly contribute to the NR-EM-LDOS.

Since the EM-LDOS is a local property, a nanoscale probe is needed for its measurement. Using electron energy loss spectroscopy (EELS)[8−11] in a scanning transmission electron microscope (STEM), it has been shown that in most cases a high energy (≥10 keV) electron beam passing through a thin sample loses its energy in proportion to the EM-LDOS (thus reflecting both the radiative and nonradiative contributions) projected along the direction of the electron beam.[12,13] The lateral component may be determined from the lateral deflection of the inelastically scattered electrons.[14] In a related technique, cathodoluminescence, where again a high-energy electron beam is used for excitation, the resulting emitted light

Received: February 19, 2020
Published: April 24, 2020

https://dx.doi.org/10.1021/acsphotonics.0c00264
ACS Photonics 2020, 7, 1280–1289

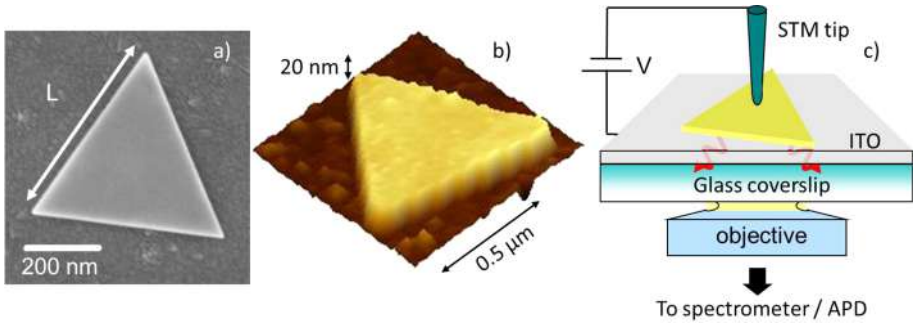

Figure 1. Sample and experimental setup. (a) Scanning electron micrograph and (b) 3D projection of a scanning tunneling microscopy image of a colloidal, triangular, gold platelet. Typical side lengths L of the studied particles are 600 to 900 nm. The platelets are 20 nm thick. For the STM image, a voltage of 0.5 V is applied and the set-point current is 0.1 nA (constant current mode). (c) Schematic of the experimental setup. The inelastic tunneling current between the STM tip and metal sample excites the plasmonic modes of the triangle platelet, which then decay radiatively. The resulting emission is collected using an oil immersion objective of high numerical aperture (NA = 1.49) and focused on either the entrance slit of a spectrometer or on an avalanche photodiode (APD).

is detected and it is the projected R-EM-LDOS that is probed,[15−18] though dark modes may also be detected through a combination of methods.[19] Other techniques for mapping the EM-LDOS are based on the use of fluorescent probes,[20−27] two-photon luminescence,[28,29] and scanning near-field optical microscopy.[30−32] Photoelectron emission microscopy is also a remarkable technique for imaging optical near-fields.[33,34]

The scanning tunneling microscope (STM) is a well-known tool for mapping the *electronic* local density of states,[35] that is, the number of electronic levels per unit volume in an infinitesimal energy range, which may even be investigated optically in certain cases.[36] While light was first seen from the STM tunnel junction as early as the late 1980s,[37] it is not until recently that an "STM-nanosource" has been used systematically to study the properties of surface plasmon polaritons (SPPs) in plasmonic gaps and nanostructures[38−45] and to locally and electrically activate directional sources of light.[46,47] Recently, considerable progress has been made toward replacing the STM-nanosource with antenna-enhanced integrated junctions for the efficient electrical excitation of plasmons and light.[48−53]

The electrical excitation of photons and plasmons in the STM is generally attributed to the inelastic tunneling current between the tip and the sample.[37,52,54] While a large majority of the tunneling electrons cross the tunnel barrier elastically, a small percentage (about 1%[54]) does so inelastically, losing part or all of the excess energy in the barrier. This released energy may excite the different modes of the system. Similar to the classical description of quantum emitters, the inelastic tunneling current responsible for this local, electrical excitation of the electromagnetic modes in a nanosystem may be represented as an oscillating point dipole. This dipole is located in the nanocavity formed between the STM tip and the sample and oriented in the direction of the tunneling current.[40,54−56] Given this description of the inelastic tunneling current and the above definition of the EM-LDOS, the question naturally arises whether the STM-nanosource may be used to probe the *electromagnetic* local density of states. More specifically, does the radiative yield of this nanosource provide a useful tool for determining the radiative component of the EM-LDOS?

In order to answer this question, we perform an experiment where the STM tip is scanned across a triangular gold platelet deposited on an ITO-covered glass substrate. At each point in the scan the emitted radiation is collected in the far field, providing a map of the STM-excitation efficiency on the sample (or "radiation map"). We also use spatially resolved electron energy loss spectroscopy (EELS) to obtain maps of the total EM-LDOS. Along with this experimental study, we perform electromagnetic calculations of the EM-LDOS and R-EM-LDOS, leading to maps of these quantities as a function of position on the triangular gold platelet. Similarly, calculations of the emitted light when an STM tip and vertical oscillating dipole are scanned over a triangular gold platelet are performed. This theoretical analysis is further used to unambiguously identify the nature of the plasmonic modes and their contributions to the near and far fields. Our joint experimental and theoretical study shows that the radiation maps obtained with an STM-nanosource are directly related to the R-EM-LDOS. Thus, the scanning tunneling microscope offers an extremely attractive method to locally, and eventually simultaneously, probe the atomic, electronic, and photonic structure of a nano-object.

RESULTS AND DISCUSSION

The spatially resolved studies of the emission of light from an STM-nanosource and the electron energy loss spectroscopy (EELS) experiments are performed on monotwinned gold crystals of triangular shape, deposited on a substrate (see the Methods section for details of the sample preparation). The substrates are either glass coverslips, 170 μm thick, covered with a conducting 85 nm thick ITO layer (for STM measurements), or 15 nm thick silicon nitride membranes (for EELS measurements). Figure 1a shows a scanning electron micrograph of such a triangle, while Figure 1b shows a three-dimensional projection of an STM topography image of such a structure. The triangles considered here have side lengths L ranging from 600 to 900 nm and are 20 nm thick.

The local excitation of the electromagnetic modes at specific locations on the triangular sample is carried out with a commercial STM head mounted on an inverted optical microscope (see Methods and Figure 1c). The inelastic tunneling current between the STM tip and metal sample generates the light that is collected through the transparent substrate using an oil immersion objective of high numerical aperture (NA = 1.49).

The emission of light is associated with the radiative decay of the electromagnetic modes of the system. In order to

https://dx.doi.org/10.1021/acsphotonics.0c00264
ACS Photonics 2020, 7, 1280−1289

identify the energies of these modes, we measure the spectra of the emitted light upon excitation with the STM-nanosource (see Figure 2). The STM-nanosource is inherently broadband[38] and depends on the applied voltage (leading to a high-energy cutoff).[57] In order to ensure that we excite the inherent resonances of the sample[58] and not the nanocavity resonances of the tip−sample system,[56,59] we use a tungsten STM tip (see Methods). Since tungsten is a nonplasmonic metal in the energy range under consideration (i.e., the real part of the permittivity is positive and the spectral response is broad and damped[60]) nanocavity resonances are thus avoided (see section 1 of the Supporting Information for further details).

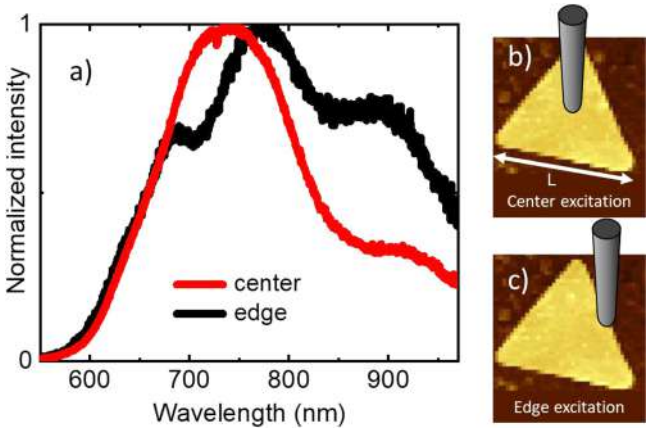

Figure 2. Experimental spectra for different excitation positions. The red curve shows the resulting light emission when the STM tunneling current excites the triangular platelet in the center of its top face, and the black curve shows the data obtained when the excitation is located on the edge of the triangle. Note that the decrease in intensity at short wavelengths ($\lesssim$575 nm) is due to the interband transitions in gold. The triangular platelet side length L is 600 nm. The spectra are normalized by their maximum values. STM parameters are $I_{\text{set-point}}$ = 0.5 nA and V = 2.8 V and the acquisition time is 300 s. Panels b and c show schematically the excitation geometries.

Figure 2 shows the resulting experimental spectra of the light emitted when the STM-nanosource is placed in the center of the upper facet (Figure 2a, red curve) or in the middle of the edge (Figure 2a, black curve) of the triangular platelet (see panels b and c of the figure for a schematic of the tip position). When the STM excitation is located in the center of the upper facet of the triangular platelet, two broad overlapping resonances may be observed in the light emission at about 730 and 910 nm, as obtained from fits to the data. When the excitation is located on the edge of the triangle, three different overlapping resonances are apparent at wavelengths of about 670, 760, and 870 nm. These results suggest that (i) the STM tunneling current indeed excites the plasmonic modes of the platelet that then decay radiatively and (ii) different modes may be selectively excited depending on the particular position of the STM tip.[46,58] We will use these spectral results to select the wavelength windows for the light emission mapping experiments.

Two wavelengths are chosen for the STM-nanosource mapping experiments. In a mapping experiment, the STM scans the particle under study in constant current mode ($I_{\text{set-point}}$ = 0.1 nA and V = 2.8 V). At each pixel in the scan, the

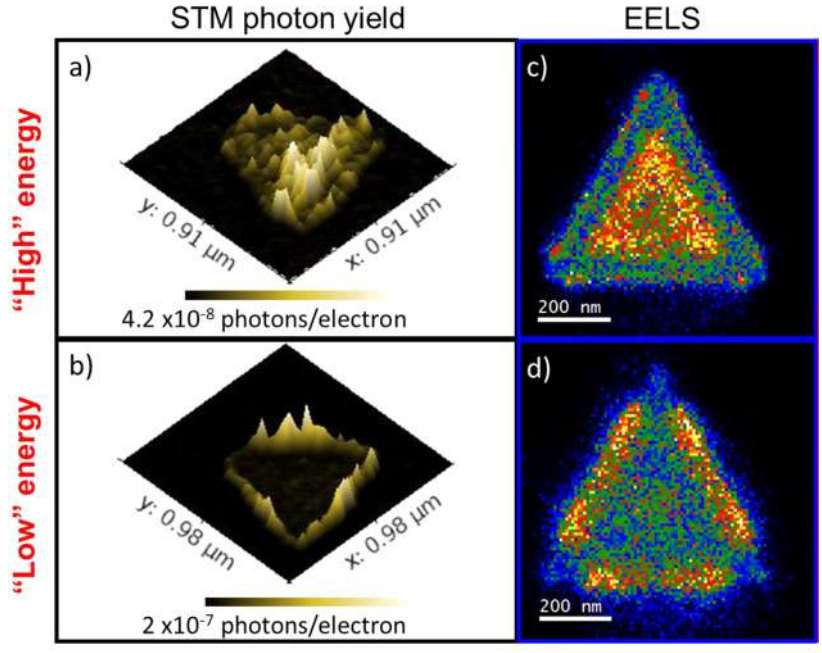

Figure 3. STM-excitation photon yield maps and EELS measurements (a, b) These photon yield maps are obtained by dividing the simultaneously acquired photon images by their corresponding current maps (see section 2 in the Supporting Information for details). The result is thus an efficiency in terms of the number of photons emitted per tunneling electron. In other words, from these results we can predict the best location for the excitation in order to get the most emission at the desired wavelength. In (a), a 750/40 nm bandpass filter is placed before the detector, while in (b), photons in the range 900 ± 20 nm are collected. The result is noticeably different for these two wavelength ranges. (c, d) Electron energy loss results. A high energy electron beam scans the particle and the energy lost by the electrons passing through the sample is measured. In (c) the number of electrons having lost energy in the 1.5−1.8 eV range as a function of e-beam position is plotted, while in (d) the energy loss range is 1.1−1.4 eV. These results match the STM-excitation images qualitatively. The triangle side length is $L \sim$ 630 nm.

https://dx.doi.org/10.1021/acsphotonics.0c00264
ACS Photonics 2020, 7, 1280−1289

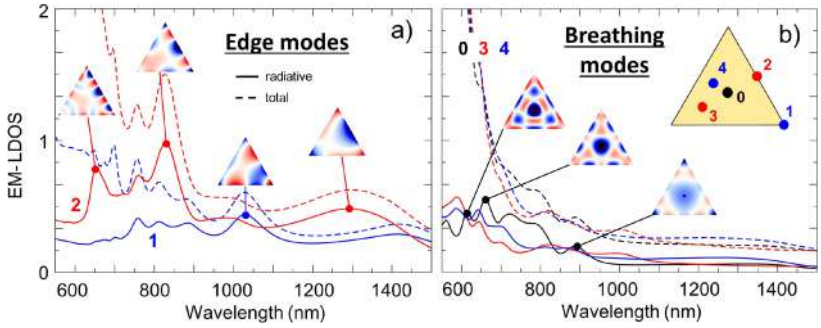

Figure 4. Calculated total local density of electromagnetic states (EM-LDOS, dotted lines) and calculated radiative local density of electromagnetic states (R-EM-LDOS, continuous lines) as a function of wavelength at different positions on the sample. For the sake of comparison, the EM-LDOS is scaled by a factor of 1.5 (EM-LDOS/1.5 is shown). (a) EM-LDOS and R-EM-LDOS as a function of wavelength at a vertex and on the edge of the platelet. (b) EM-LDOS and R-EM-LDOS as a function of wavelength in and near the center of the platelet. The position at which each curve is calculated is shown in the inset of panel (b). The surface charge densities of the main modes are displayed above their corresponding peaks in the R-EM-LDOS. The triangle side length used in these calculations is L = 650 nm.

topography, tunneling current, and number of photons emitted into the substrate in the collection angle of the objective are recorded (see Supporting Information, section 2 for details). The photodetector is an avalanche photodiode in front of which different bandpass filters are placed so that wavelength-dependent maps may be obtained. The light emission maps are divided by the simultaneously recorded tunnel current signal in order to obtain the excitation efficiency or photon yield (in photons/electron).

Plotting the emitted light per electron as a function of STM excitation position for two different energy ranges yields very different results. In Figure 3a, the number of photons emitted per electron in a wavelength range of 750 ± 20 nm as a function of excitation position is shown, while Figure 3b shows the same for a wavelength range of 900 ± 20 nm. For the higher energy/shorter wavelength range, more light is emitted per electron when the STM tip is located in the center of the upper face of the platelet, while for the lower energy/longer wavelength range, the most efficient excitation of light occurs when the STM tip is located on the edge of the nanoparticle. This striking contrast would suggest that different types of electromagnetic modes are excited in each case.

In order to gain further insight into the character of the plasmonic modes contributing to the emission maps obtained with the STM-nanosource, and to investigate the link between these results and the electromagnetic EM-LDOS, similar experiments are performed using electron energy loss spectroscopy (EELS; see Methods and section 3 of the Supporting Information). Looking at the EELS data in Figure 3c,d for a similar triangular platelet, we obtain a result that shows similar trends as in the case of the STM-nanosource excitation: considering a high energy/short wavelength range, a strong signal is measured when the excitation (a high energy (100 keV) electron beam) is incident on the flat upper surface of the triangle platelet; for a low energy/long wavelength range, the signal is most significant when the excitation is along the triangle edge.

Since EELS is a loss spectroscopy, it reflects the total EM-LDOS projected along the axis of the incoming electron beam;[12] that is, it is equally sensitive to both the dark (i.e., nonradiative) and bright (or radiative) modes of the system. In the STM excitation experiment, however, the emitted light is detected in the far field. This would suggest that the STM-nanosource experiments are only sensitive to the radiative R-EM-LDOS, whose leading contribution is from the bright modes of the sample. The dark modes of the triangular platelet should only contribute to the observed light emission maps if the STM tip or retardation effects allow these modes to couple to the far field. A simulation of the STM experiment is thus necessary to interpret the STM-nanosource results and to further investigate the link between the experimental data and the EM-LDOS.

The first step in the theoretical analysis is the determination of the total and radiative local density of electromagnetic states as well as the electromagnetic (EM) modes of the triangular platelets, so that the nature of the EM modes excited by the tunneling current may be identified. In Figure 4 the calculated wavelength dependence of the EM-LDOS (dashed curves) and R-EM-LDOS (continuous curves) of a triangular platelet is shown for different positions of the excitation point dipole. Here, the R-EM-LDOS is obtained by calculating the emission in all directions when a point dipole with a flat spectrum is placed at different lateral positions 1 nm above the triangle (see the inset of Figure 4b). Meanwhile, the total EM-LDOS is obtained from the electric field at the position of the dipole.[2]

The resonance peaks in the EM-LDOS and R-EM-LDOS are associated with surface charge density distributions on the sample of specific symmetry (see Figure 4). Based on these symmetry considerations, two main sets of plasmonic modes for the triangular platelet are identified: edge and breathing modes, in accordance with previous classifications in the literature.[61−67] The edge modes contribute preferentially to the EM-LDOS above the vertices and edges of the triangle (Figure 4a), and the number of nodes in the induced charge density distribution of these modes increases with decreasing wavelength.[61−63] The low-order modes of this type appear at long wavelengths and include the dipolar plasmon resonance (located above 2500 nm) and the quadrupolar plasmon resonance at 1300 nm (excitation in the center of the edge, point 2). These edge modes are clearly radiative: consider for example the lowest order edge mode for which the charge density distribution is shown in Figure 4a (λ = 1300 nm); the radiative R-EM-LDOS is more than half the value of the total EM-LDOS (recall that the total EM-LDOS is divided by a factor of 1.5 in Figure 4).

The second set of EM modes contributes preferentially to the EM-LDOS above the center of the platelet (Figure 4b). In this case, the induced charge distribution is concentric on the platelet facets. This is characteristic of breathing or film-like modes[61−66] launched on a gold film by a vertical oscillating

https://dx.doi.org/10.1021/acsphotonics.0c00264
ACS Photonics 2020, 7, 1280−1289

dipole and discretized by the reflections at the platelet boundaries. By symmetry, these breathing modes have no net induced dipole moment and are, in general, much less radiative as compared to the edge modes. This again may be seen by comparing the total and radiative EM-LDOS at for example 900 nm (lowest order breathing mode for which the charge density distribution is shown in Figure 4b). In this case, the total EM-LDOS is equal to more than a factor of 3 times the radiative R-EM-LDOS. The fact that the edge modes are clearly more radiative than the breathing modes (for $\lambda > 600$ nm) is confirmed in section 4 of the Supporting Information and in Figure 5a.

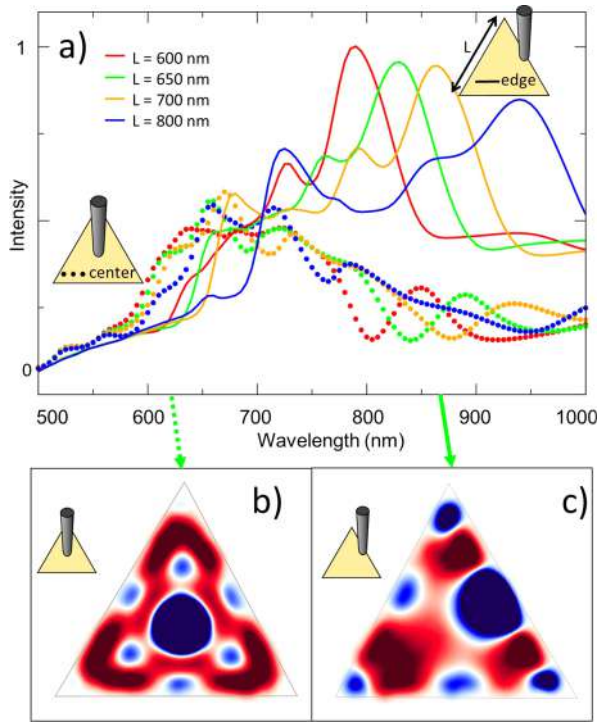

Figure 5. Calculated light emission spectra for different excitation positions and triangular platelet sizes. (a) Calculated spectra. Dotted lines: results for the STM tip located in the center of the triangle face. Continuous curves: results for the STM tip located in the center of the triangle edge. The platelets side lengths are varied from $L = 600$ to 800 nm, as indicated in the inset. (b, c) Surface charge density induced at a wavelength of (b) 620 and (c) 860 nm for the tip location indicated in the insets. The calculations are performed with a tip (radius 40 nm, length 400 nm) placed 2 nm above the platelet surface (substrate index of refraction is 2).

At wavelengths of $\lambda \lesssim 800$ nm, higher-order plasmonic modes are excited. These higher-order modes involve rapidly oscillating charge densities and higher-order multipole moments, thus reducing the coupling of these modes to the far field. At the same time, however, we see that the total EM-LDOS of the breathing modes diverges for shorter wavelengths (see Figure 4b). Since the total EM-LDOS increases drastically, the radiative R-EM-LDOS increases proportionally. In the competition between these two effects (reduced far-field coupling and the increase in the total number of electromagnetic modes), the increase in the total EM-LDOS dominates, leading to higher values of the radiative R-EM-LDOS at shorter wavelengths as compared to longer wavelengths. In fact, at these shorter wavelengths, the R-EM-LDOS of the breathing modes is comparable to the R-EM-LDOS values of the edge modes (consider, for example, the continuous blue curves in Figure 4a,b).

The connection between the R-EM-LDOS and the experimental spectra shown in Figure 2 is made in Figure 5a. Here we calculate the spectrum of the light emitted into the substrate when the STM-nanosource excites the platelet; as opposed to the previous calculation for the R-EM-LDOS, these results include the STM tip, exclude the emission in the half space above the platelet, and take into account the STM excitation spectrum[57] (see Methods and section 5 in the SI). The theoretical results in Figure 5a are obtained for triangles of different side lengths and for the two relevant tip positions addressed experimentally.

Comparing Figures 4 and 5a, it may be seen that the emission spectra calculated for the complete STM system (platelet plus tip) closely resembles the R-EM-LDOS of the isolated triangular platelet (i.e., no tip included; see also section 5 in the SI for a plot of the data of Figures 4 and 5 on the same graph). This demonstrates (i) the nonperturbing role of the STM tip, as outlined earlier; (ii) the similarity, up to a scaling factor, between the R-EM-LDOS and the emission into the substrate; and (iii) the excitation of the different types of modes as a function of tip position. While the peaks in the simulated spectra are narrower than in the experiment, probably due to the idealization of the system used for the calculations (see section 6 in the SI), the same general trend emerges from the calculated and measured data.

Figure 5b,c displays the calculated surface charge densities for the center and edge tip excitation positions at two specific energies ($\lambda = 620$ and 860 nm, respectively). As for Figure 5a, the differences in the calculation as compared to the insets of Figure 4 involve the inclusion of the STM tip and the STM-nanosource excitation spectrum and the exclusion of the light emitted above the substrate. Once again, good agreement between the R-EM-LDOS (insets to Figure 4) and the STM excitation calculations (Figure 5b,c) is seen: at low energies and excitation on the edge (Figure 5c), the result is reminiscent of an edge mode. When the excitation is at higher energy and in the center of the platelet (Figure 5b), the resulting symmetric surface charge distribution resembles that of a breathing mode.

As pointed out previously, in the light emission experiments from an STM-nanosource, light is detected in the far field; thus, this technique is expected to probe the radiative EM-LDOS of the sample under study. In order to confirm this, interpret the experimental results of Figure 3 and, in particular, test for possible tip or substrate effects that might perturb the link between the R-EM-LDOS and the results of the STM experiments, we perform calculations of the total EM-LDOS, of the R-EM-LDOS, and of the photon emission as a function of position for selected wavelengths. Each selected wavelength corresponds to the excitation of a different plasmonic mode of the platelet.

From the calculated total EM-LDOS, R-EM-LDOS, and intensity maps in Figure 6 it follows that, for longer wavelengths (820−1300 nm), the edge plasmon modes are predominantly excited, as seen from the intense bright spots along the edges and vertices of the platelet. The strong radiative nature of the excited edge modes explains the close similarity between the EM-LDOS, R-EM-LDOS, and intensity maps at these wavelengths. The dominance of the radiative edge modes is also behind the good agreement between the

https://dx.doi.org/10.1021/acsphotonics.0c00264
ACS Photonics 2020, 7, 1280−1289

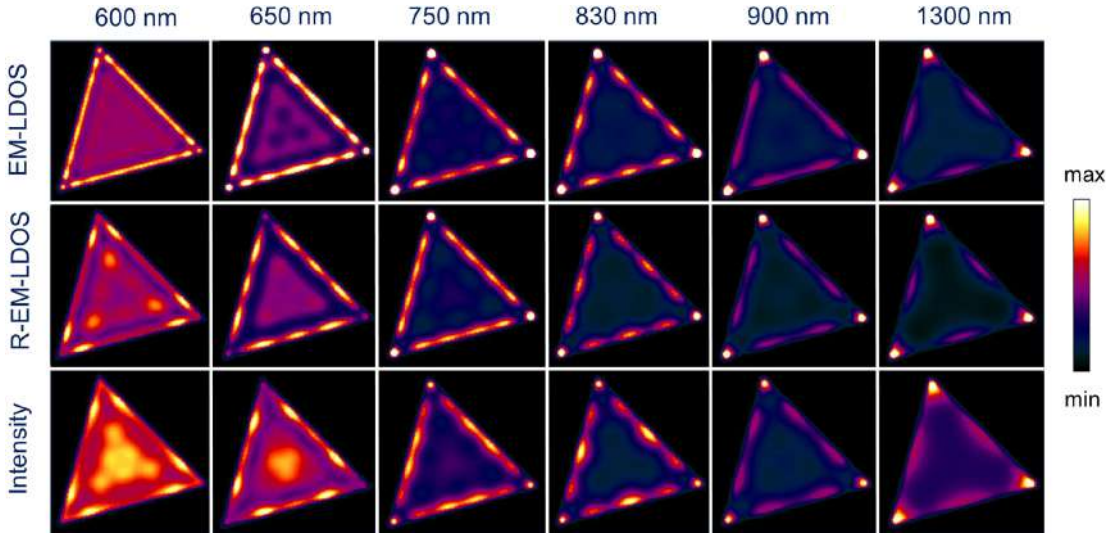

Figure 6. Calculated energy-resolved maps of the EM-LDOS, R-EM-LDOS, and of the intensity of the light emitted by the tunneling STM-nanosource when scanned over a triangular platelet with side length L = 650 nm. The EM-LDOS is calculated 1 nm above the upper face of the platelet. The STM tip scans the upper face of the platelet at a constant tip−surface distance of 2 nm. Different columns correspond to the maps obtained for different radiation wavelengths as indicated.

calculations and the STM and EELS measurements at longer wavelengths (see Figure 3b,d).

As the wavelength decreases from 750 to 600 nm, the signal in the center of the maps increases, reflecting the increasing role of the breathing modes (see the left-hand side of Figure 6). This is in full agreement with the STM and EELS measurements of Figure 3a and Figure 3c. Comparing the R-EM-LDOS and EM-LDOS data in the leftmost columns of Figure 6 we observe (i) a different structure in the center; (ii) different relative intensities between the center and edges and (iii) a different number of nodes along the edge. This is due to the fact that there are many different higher-order modes at these short wavelengths and that these different modes contribute differently to the R-EM-LDOS and EM-LDOS. Note that such subtle differences are not clearly discernible in Figure 3 (too small signal-to-noise in the experimental data).

The third row of Figure 6 shows the calculated photon emission maps (i.e., the emission into the substrate taking into account the presence of the tip and the STM-excitation spectrum). These results match the radiative R-EM-LDOS: the number of nodes along the triangle edges as well as the structure in the center of the platelet are well reproduced in both types of images. Note, however, that the relative intensities of the different contributions are not always the same in both cases. This is attributed to the presence of the STM tip. While it has been shown that a nonplasmonic tip does not perturb the energy spectrum of the inherent modes of the particle (see Figures 4 and 5 or sections 1 and 5 in the Supporting Information), it appears that the tip alters the mode coupling to the far field, as seen from the increased intensity from the center of the photon emission maps. In particular, the tip enhances the far-field coupling of the numerous breathing modes at short wavelengths.

SUMMARY AND CONCLUSIONS

In summary, we have used the inelastic tunneling current from a scanning tunneling microscope working in air to locally and electrically excite the plasmonic modes of a triangular gold platelet. The light resulting from the radiative decay of these plasmonic modes is collected through the transparent substrate. Both tip position-dependent light emission spectra as well as emission maps have been acquired, revealing that breathing modes of higher energy are more efficiently excited when the STM tip is positioned in the center of the upper face of the platelet, while edge modes at lower energies are preferably excited when the STM tip is positioned on an edge. Acquiring EELS maps on similar triangular platelets yields qualitatively similar results. The theoretical study of STM-induced light emission reproduces the main experimental trends and confirms the excitation of breathing and edge modes of the nanoparticle, associated with particular tip positions and emission energies. More importantly, a detailed comparison of the calculated total EM-LDOS and the radiative R-EM-LDOS reveals subtle differences in the corresponding mapping of each mode, depending on its radiative nature. Thus, the scanning tunneling microscope may be considered not only a tool for mapping the electronic density of states in its usual operation mode, but also for investigating the radiative electromagnetic local density of states when the emitted light is collected. This work introduces a new technique for probing the radiative R-EM-LDOS and may be applied to obtain relevant information on nanoantennas,[68−71] improved nanoplatforms for surface-enhanced Raman scattering (SERS),[72−74] surface-enhanced fluorescence,[75,76] single photon emission,[71] and strong coupling in hybrid plasmonic-emitter systems.[77]

METHODS

Samples. The triangular gold platelets (monotwinned gold crystals, side length L = 600−900 nm, thickness 20 ± 1 nm) are synthesized by colloidal chemistry. A modified seed-mediated growth protocol, initially proposed by Mirkin's group, is used with cetyltrimethylammonium bromide (CTAB) as the stabilizing and structure-directing agent.[78] Here, contrary to the referenced protocol, the CTAB concentration is increased by a factor of 2 (0.1 M instead of 0.05 M), so that a mixture of thicker triangular and hexagonal platelets is obtained (20 nm instead of 9 nm). A seed solution is first

https://dx.doi.org/10.1021/acsphotonics.0c00264
ACS Photonics 2020, 7, 1280−1289

prepared by adding an ice-cold $NaBH_4$ solution (0.42 mL, 10 mM) into an aqueous solution composed of a mixture of $HAuCl_4$ (92 μL, 10 mM) and CTAB (7 mL, 100 mM). The growth solution is prepared by successively mixing 7.3 mL of a 1 M CTAB/50 μM NaI solution with 195 μL of $HAuCl_4$ (0.01 M), 280 μL of ascorbic acid (0.016 M), and finally, 43 μL of NaOH (0.1 M). Adding the seeds (2 μL of the 100-fold diluted seed solution) initiates the particle synthesis reaction, which occurs for 5 h at 40 °C. The platelets are then purified through selective sedimentation at the bottom of the reaction vessel owing to a depletion-induced interaction.[79] The chemicals used are cetyltrimethylammonium bromide (CTAB ≥ 98%), chloroauric acid ($HAuCl_4 \cdot 3H_2O$), sodium borohydride ($NaBH_4$, 99%), ascorbic acid (99%), and sodium iodide NaI (99%). They are purchased from Sigma and used as received. Deionized water is used for all experiments.

The substrates used are either 170 μm thick glass coverslips covered with an 85 nm thick indium−tin-oxide (ITO) layer (SOLEMS, Palaiseau, France) or 15 nm thick transmission electron microscope silicon nitride membrane window grids (Ted Pella). The final samples are prepared by depositing a diluted drop of the Au platelet solution on the substrate. After drying, the sample is copiously washed with ethanol, dried, and then cleaned by UV/ozone to remove any organic residue.

STM/Optical Microscopy Setup. The commercial STM head is from JPK Instruments (NanoWizard 3). STM tips are made of tungsten using electrochemical etching (typical radii ∼ 35 nm). The STM is mounted on top of an inverted optical microscope (Nikon Eclipse Ti−U) equipped with an oil immersion objective (Nikon CFI Apochromat 100× 1.49 NA TIRF objective). The resulting light from the STM-excitation experiments is collected through the transparent substrate. For the spectral measurements, a real plane image of the sample is projected onto the slit opening of a spectrometer and integrated for 300 s (STM parameters are $I_{\text{set-point}}$ = 0.5 nA and V = 2.8 V). All reported spectra have been corrected for system response. The imaging spectrometer is from Horiba Jobin Yvon (iHR320 spectrometer with a Synapse CCD detector). For the mapping, all the light from a 250 μm^2 area is detected by an avalanche photodiode (from Excelitas, dark count as low as 5 counts/s) and integrated for each pixel by the STM controller. A bandpass filter (center wavelength 750 nm and bandwidth 40 nm, or 900 nm center wavelength and again a bandwidth of 40 nm) is placed before the detector. As a result, the topography image, tunneling current map, and photon map for a particular wavelength range may be acquired simultaneously. In the STM experiments, a (positive) voltage is applied to the sample and the tip is grounded. This voltage is either 0.5 V for imaging or 2.8 V for excitation (a voltage of >1.5 V is necessary for emission in the visible). These measurements are performed in constant current mode with a feedback loop, which maintains the measured tunneling current nominally constant at a value of 0.1 nA. Note that triangle side lengths L measured by STM are most likely overestimated due to convolution with the tip. All of the reported measurements are carried out in air under standard laboratory conditions. As a result, a thin water layer exists on both the sample and the tip. Details on the specificities of the STM-excitation of plasmons in air may be found in the reference Rogez et al.[80]

Electron Energy Loss Spectroscopy. STEM-EELS measurements are performed using a Vacuum Generator HB501 scanning transmission electron microscope (STEM) operated at 100 kV, fitted with a cold field emission gun and a homemade electron energy loss spectrometer (EELS) detection system. The electron probe size is a few nanometers and the EEL spectrometer energy dispersion is 20 meV/channel. The data is collected in the spectral image mode where high-angle annular dark field (HAADF) signals and EEL spectra are collected simultaneously pixel by pixel while scanning. At the end of a scan, both a HAADF image and a spectrum image (EEL spectrum at each pixel of the scan) are generated that can be compared pixel by pixel. By means of a spectrum image, filtered maps are created by plotting the EEL signal intensity of each pixel in a chosen energy range. Typical acquisition times per pixel are 5 ms and spectral image data sets are 100 × 100 pixels large. Spectral alignment and Richardson-Lucy deconvolution are used in order to improve the energy resolution from ∼0.3 to ∼0.1 eV (zero loss peak full-width at half-maximum) using the Hyperspy software.[81]

Simulations. Three-dimensional electrodynamic calculations are performed for a unitary harmonic point source emitter with current density given by $\vec{j} = \hat{u}\delta(\vec{r} - \vec{r_0})$, where the unitary vector $\hat{u}$ defines the polarization of the source. The position $\vec{r_0}$ of the point source is 1 nm above the upper face of the platelet for the calculations. In the case of the photon maps, an STM tip is also included 1 nm above the point source. Unless otherwise stated, we consider that the tunneling source is oriented perpendicularly to the platelet face along the symmetry axis of the tip. The finite element method as implemented in the frequency domain using the radio frequency module of the commercial COMSOL Multiphysics software[82] is used. For the photon emission spectral calculations, the resulting calculated spectra are multiplied by a factor of $(eV - \hbar\omega)$ (where e is the charge of an electron, V is the applied voltage between the tip and sample, and ω is the photon angular frequency) in order to take into account the inelastic tunneling electron probability as a function of energy.[57,83] For the calculation of the EM-LDOS we consider that it is dominated by the electromagnetic modes of the platelet, and we use the expression for the change of the rate of the radiative and nonradiative energy dissipation by the point emitter due to the presence of the metal.[84]

$$\Gamma = -\frac{1}{2} Re\{\hat{u}\cdot\vec{E}(\vec{r_0})\} \tag{1}$$

where $\vec{E}(\vec{r_0})$ is the electric field (at the position of the point source emitter) created by the gold platelet (the calculations are performed without an STM tip). $Re\{Z\}$ stands for the real part of the complex quantity Z. On the other hand, the change of the power dissipated by the unitary point source can be presented through the electromagnetic density of states of the metal, $\rho_{\hat{u}}^{m}(\vec{r_0}, \omega)$, as follows:[2]

$$\Gamma = \frac{\pi}{4\epsilon_0}\rho_{\hat{u}}^{m}(\vec{r_0}, \omega) \tag{2}$$

This immediately leads to $\rho_{\hat{u}}^{m}(\vec{r_0}, \omega)$ from the calculated $Re\{\hat{u}\vec{E}(\vec{r_0})\}$. We consider that $\rho_{\hat{u}}^{m}(\vec{r_0}, \omega) \gg \rho_{\hat{u},0}(\vec{r_0}, \omega)$, where $\rho_{\hat{u},0}(\vec{r_0}, \omega) = \frac{\omega^2}{3\pi^2 c^3}$ is the projected EM-LDOS in vacuum (ω is the angular frequency and c is the speed of light).

For the R-EM-LDOS mapping results, the Poynting vector in the far field is integrated over a full sphere enclosing the system (the calculations are performed without an STM tip).

https://dx.doi.org/10.1021/acsphotonics.0c00264
ACS Photonics 2020, 7, 1280−1289

For the photon emission spectra and photon emission maps the calculations are performed for the unitary harmonic point source emitter placed in the junction between the STM tip and platelet surface, and the Poynting vector in the far field is integrated over a half sphere beneath the substrate.

The gold triangle (20 nm thick) is considered equilateral with rounded vertices (radius of curvature 5 nm). Side lengths of 600−900 nm are considered. The index of refraction of gold that is used is from Johnson and Christy.[85] The substrate is represented either by a semi-infinite space with refraction index $n = 2$ below the triangle structure or, in the case of the surface charge density calculations of Figure 5, by a disk of radius 1600 nm and of thickness 200 nm (index of refraction is 2), with air above and below. The full environment is a sphere of radius 2000 nm, surrounded by a 300 or 600 nm thick perfectly matched layer. The tungsten tip (index of refraction from Rakić et al.[60]) is represented by a solid cone which has an opening angle of $\tan\theta = (1/6)$ and whose end is replaced by a sphere of radius 40 nm. The length of the tip is 400 nm. See section 1 of the Supporting Information for results with different values for the tip radius and length.

■ ASSOCIATED CONTENT

Supporting Information

The Supporting Information is available free of charge at https://pubs.acs.org/doi/10.1021/acsphotonics.0c00264.

1. Calculated spectra and tip effects; 2. STM-nanosource mapping experiments; 3. Electron energy loss spectroscopy: spectra and spatially resolved maps; 4. Spectra as a function of triangle side length; 5. Comparison of the calculated emission above and below the substrate and the R-EM-LDOS; 6. Triangle shapes and dimensions: HAADF STEM images (PDF)

■ AUTHOR INFORMATION

Corresponding Author

Elizabeth Boer-Duchemin − *Université Paris-Saclay, CNRS, Institut des Sciences Moléculaires d'Orsay (ISMO), 91405 Orsay, France;* orcid.org/0000-0002-3657-8424; Email: elizabeth.boer-duchemin@u-psud.fr

Authors

Shuiyan Cao − *Department of Applied Physics, Nanjing University of Aeronautics and Astronautics, Nanjing, China; Université Paris-Saclay, CNRS, Institut des Sciences Moléculaires d'Orsay (ISMO), 91405 Orsay, France*

Mario Zapata-Herrera − *Materials Physics Center CSIC-UPV/EHU and Donostia International Physics Center DIPC, 20018 Donostia-San Sebastián, Spain*

Alfredo Campos − *Université Paris-Saclay, CNRS, Laboratoire de Physique des Solides (LPS), 91405 Orsay, France;* orcid.org/0000-0001-7921-8309

Eric Le Moal − *Université Paris-Saclay, CNRS, Institut des Sciences Moléculaires d'Orsay (ISMO), 91405 Orsay, France*

Sylvie Marguet − *Université Paris-Saclay, CEA, CNRS, NIMBE, CEA Saclay, Gif-sur-Yvette, France*

Gérald Dujardin − *Université Paris-Saclay, CNRS, Institut des Sciences Moléculaires d'Orsay (ISMO), 91405 Orsay, France*

Mathieu Kociak − *Université Paris-Saclay, CNRS, Laboratoire de Physique des Solides (LPS), 91405 Orsay, France;* orcid.org/0000-0001-8858-0449

Javier Aizpurua − *Materials Physics Center CSIC-UPV/EHU and Donostia International Physics Center DIPC, 20018 Donostia-San Sebastián, Spain;* orcid.org/0000-0002-1444-7589

Andrei G. Borisov − *Université Paris-Saclay, CNRS, Institut des Sciences Moléculaires d'Orsay (ISMO), 91405 Orsay, France;* orcid.org/0000-0003-0819-5028

Complete contact information is available at: https://pubs.acs.org/10.1021/acsphotonics.0c00264

Author Contributions

[§]These authors contributed equally to this work.

Notes

The authors declare no competing financial interest.

■ ACKNOWLEDGMENTS

S.C. acknowledges the financial support of the China Scholarship Council (CSC; No. 201304910386). M.Z.-H. acknowledges the financial support of the European Union under the Project H2020 FETOPEN-2016-2017 "FEMTO-TERABYTE" (Project No. 737093) and the "Colombian Administrative Department of Science, Technology and Innovation" - COLCIENCIAS under its "Estancias Post-doctorales 784-2017" call. He also acknowledges the hospitality of the Institute des Sciences Moléculaires d'Orsay and Dr. Nuno de Sousa for his guidance and support using COMSOL Multiphysics. S.M. was supported by the HAPPLE grant (French National Research Agency: ANR-12-BS10-0016). This work is partially funded by the Conseil Régional, Île-de-France (DIM Nano-K). J.A. acknowledges Project FIS2016-80174-P of the Spanish MICINN and Project IT1164-19 of the Basque Government.

■ REFERENCES

(1) Vahala, K. J. Optical microcavities. *Nature* **2003**, *424*, 839.

(2) Carminati, R.; Caze, A.; Cao, D.; Peragut, F.; Krachmalnicoff, V.; Pierrat, R.; De Wilde, Y. Electromagnetic density of states in complex plasmonic systems. *Surf. Sci. Rep.* **2015**, *70*, 1−41.

(3) Callahan, D. M.; Munday, J. N.; Atwater, H. A. Solar Cell Light Trapping beyond the Ray Optic Limit. *Nano Lett.* **2012**, *12*, 214−218.

(4) Dousse, A.; Suffczyński, J.; Beveratos, A.; Krebs, O.; Lemaître, A.; Sagnes, I.; Bloch, J.; Voisin, P.; Senellart, P. Ultrabright source of entangled photon pairs. *Nature* **2010**, *466*, 217.

(5) Hoang, T. B.; Akselrod, G. M.; Argyropoulos, C.; Huang, J.; Smith, D. R.; Mikkelsen, M. H. Ultrafast spontaneous emission source using plasmonic nanoantennas. *Nat. Commun.* **2015**, *6*, 7788.

(6) Joulain, K.; Carminati, R.; Mulet, J.-P.; Greffet, J.-J. Definition and measurement of the local density of electromagnetic states close to an interface. *Phys. Rev. B: Condens. Matter Mater. Phys.* **2003**, *68*, 245405.

(7) Novotny, L.; Hecht, B. *Principles of Nano-Optics*; Cambridge University Press, 2006.

(8) Nelayah, J.; Gu, L.; Sigle, W.; Koch, C. T.; Pastoriza-Santos, I.; Liz-Marzán, L. M.; van Aken, P. A. Direct imaging of surface plasmon resonances on single triangular silver nanoprisms at optical wavelength using low-loss EFTEM imaging. *Opt. Lett.* **2009**, *34*, 1003−1005.

(9) Talebi, N.; Sigle, W.; Vogelgesang, R.; Koch, C. T.; Fernández-López, C.; Liz-Marzán, L. M.; Ögüt, B.; Rohm, M.; van Aken, P. A. Breaking the Mode Degeneracy of Surface Plasmon Resonances in a Triangular System. *Langmuir* **2012**, *28*, 8867−8873.

(10) Kociak, M.; Stephan, O. Mapping plasmons at the nanometer scale in an electron microscope. *Chem. Soc. Rev.* **2014**, *43*, 3865−3883.

(11) Hörl, A.; Haberfehlner, G.; Trügler, A.; Schmidt, F.-P.; Hohenester, U.; Kothleitner, G. Tomographic imaging of the photonic environment of plasmonic nanoparticles. *Nat. Commun.* **2017**, *8*, 37.
(12) Garcia de Abajo, F. J.; Kociak, M. Probing the photonic local density of states with electron energy loss spectroscopy. *Phys. Rev. Lett.* **2008**, *100*, 106804.
(13) Hohenester, U.; Ditlbacher, H.; Krenn, J. R. Electron-Energy-Loss Spectra of Plasmonic Nanoparticles. *Phys. Rev. Lett.* **2009**, *103*, 106801.
(14) Krehl, J.; Guzzinati, G.; Schultz, J.; Potapov, P.; Pohl, D.; Martin, J.; Verbeeck, J.; Fery, A.; Buechner, B.; Lubk, A. Spectral field mapping in plasmonic nanostructures with nanometer resolution. *Nat. Commun.* **2018**, *9*, 4207.
(15) Kuttge, M.; Vesseur, E. J. R.; Koenderink, A. F.; Lezec, H. J.; Atwater, H. A.; Garcia de Abajo, F. J.; Polman, A. Local density of states, spectrum, and far-field interference of surface plasmon polaritons probed by cathodoluminescence. *Phys. Rev. B: Condens. Matter Mater. Phys.* **2009**, *79*, 113405.
(16) Sapienza, R.; Coenen, T.; Renger, J.; Kuttge, M.; van Hulst, N. F.; Polman, A. Deep-subwavelength imaging of the modal dispersion of light. *Nat. Mater.* **2012**, *11*, 781−787.
(17) Losquin, A.; Kociak, M. Link between Cathodoluminescence and Electron Energy Loss Spectroscopy and the Radiative and Full Electromagnetic Local Density of States. *ACS Photonics* **2015**, *2*, 1619−1627.
(18) Losquin, A.; Zagonel, L. F.; Myroshnychenko, V.; Rodrguez-González, B.; Tencé, M.; Scarabelli, L.; Förstner, J.; Liz-Marzán, L. M.; García de Abajo, F. J.; Stéphan, O.; Kociak, M. Unveiling Nanometer Scale Extinction and Scattering Phenomena through Combined Electron Energy Loss Spectroscopy and Cathodoluminescence Measurements. *Nano Lett.* **2015**, *15*, 1229−1237.
(19) Myroshnychenko, V.; Nishio, N.; García de Abajo, F. J.; Förstner, J.; Yamamoto, N. Unveiling and Imaging Degenerate States in Plasmonic Nanoparticles with Nanometer Resolution. *ACS Nano* **2018**, *12*, 8436−8446.
(20) Hoogenboom, J. P.; Sanchez-Mosteiro, G.; Colas des Francs, G.; Heinis, D.; Legay, G.; Dereux, A.; van Hulst, N. F. The Single Molecule Probe: Nanoscale Vectorial Mapping of Photonic Mode Density in a Metal Nanocavity. *Nano Lett.* **2009**, *9*, 1189−1195.
(21) Beams, R.; Smith, D.; Johnson, T. W.; Oh, S.-H.; Novotny, L.; Vamivakas, A. N. Nanoscale Fluorescence Lifetime Imaging of an Optical Antenna with a Single Diamond NV Center. *Nano Lett.* **2013**, *13*, 3807−3811.
(22) Ropp, C.; Cummins, Z.; Nah, S.; Fourkas, J. T.; Shapiro, B.; Waks, E. Nanoscale imaging and spontaneous emission control with a single nano-positioned quantum dot. *Nat. Commun.* **2013**, *4*, 1447.
(23) Krachmalnicoff, V.; Cao, D.; Caze, A.; Castanie, E.; Pierrat, R.; Bardou, N.; Collin, S.; Carminati, R.; De Wilde, Y. Towards a full characterization of a plasmonic nanostructure with a fluorescent near-field probe. *Opt. Express* **2013**, *21*, 11536−11545.
(24) Schell, A. W.; Engel, P.; Werra, J. F. M.; Wolff, C.; Busch, K.; Benson, O. Scanning Single Quantum Emitter Fluorescence Lifetime Imaging: Quantitative Analysis of the Local Density of Photonic States. *Nano Lett.* **2014**, *14*, 2623−2627.
(25) Cao, D.; Caze, A.; Calabrese, M.; Pierrat, R.; Bardou, N.; Collin, S.; Carminati, R.; Krachmalnicoff, V.; De Wilde, Y. Mapping the Radiative and the Apparent Nonradiative Local Density of States in the Near Field of a Metallic Nanoantenna. *ACS Photonics* **2015**, *2*, 189−193.
(26) Aigouy, L.; Caze, A.; Gredin, P.; Mortier, M.; Carminati, R. Mapping and Quantifying Electric and Magnetic Dipole Luminescence at the Nanoscale. *Phys. Rev. Lett.* **2014**, *113*, 076101.
(27) Cuche, A.; Berthel, M.; Kumar, U.; Colas des Francs, G.; Huant, S.; Dujardin, E.; Girard, C.; Drezet, A. Near-field hyperspectral quantum probing of multimodal plasmonic resonators. *Phys. Rev. B: Condens. Matter Mater. Phys.* **2017**, *95*, 121402.
(28) Viarbitskaya, S.; Teulle, A.; Marty, R.; Sharma, J.; Girard, C.; Arbouet, A.; Dujardin, E. Tailoring and imaging the plasmonic local density of states in crystalline nanoprisms. *Nat. Mater.* **2013**, *12*, 426−432.
(29) Imaeda, K.; Hasegawa, S.; Imura, K. Static and Dynamic Near-Field Measurements of High-Order Plasmon Modes Induced in a Gold Triangular Nanoplate. *J. Phys. Chem. Lett.* **2018**, *9*, 4075−4081.
(30) Chicanne, C.; David, T.; Quidant, R.; Weeber, J. C.; Lacroute, Y.; Bourillot, E.; Dereux, A.; Colas des Francs, G.; Girard, C. Imaging the Local Density of States of Optical Corrals. *Phys. Rev. Lett.* **2002**, *88*, 097402.
(31) Rang, M.; Jones, A. C.; Zhou, F.; Li, Z.-Y.; Wiley, B. J.; Xia, Y.; Raschke, M. B. Optical Near-Field Mapping of Plasmonic Nanoprisms. *Nano Lett.* **2008**, *8*, 3357−3363.
(32) Imaeda, K.; Hasegawa, S.; Imura, K. Imaging of Plasmonic Eigen Modes in Gold Triangular Mesoplates by Near-Field Optical Microscopy. *J. Phys. Chem. C* **2018**, *122*, 7399−7409.
(33) Awada, C.; Popescu, T.; Douillard, L.; Charra, F.; Perron, A.; Yockell-Lelièvre, H.; Baudrion, A.-L.; Adam, P.-M.; Bachelot, R. Selective Excitation of Plasmon Resonances of Single Au Triangles by Polarization-Dependent Light Excitation. *J. Phys. Chem. C* **2012**, *116*, 14591−14598.
(34) Frank, B.; Kahl, P.; Podbiel, D.; Spektor, G.; Orenstein, M.; Fu, L.; Weiss, T.; Horn-von Hoegen, M.; Davis, T. J.; Meyer zu Heringdorf, F.-J.; Giessen, H. Short-range surface plasmonics: Localized electron emission dynamics from a 60-nm spot on an atomically flat single-crystalline gold surface. *Science Advances* **2017**, *3*, e1700721.
(35) Tersoff, J.; Hamann, D. R. Theory of the scanning tunneling microscope. *Phys. Rev. B: Condens. Matter Mater. Phys.* **1985**, *31*, 805−813.
(36) Schull, G.; Becker, M.; Berndt, R. Imaging Confined Electrons with Plasmonic Light. *Phys. Rev. Lett.* **2008**, *101*, 136801.
(37) Gimzewski, J. K.; Sass, J. K.; Schlitter, R. R.; Schott, J. Enhanced Photon-emission In Scanning Tunnelling Microscopy. *Europhys. Lett.* **1989**, *8*, 435−440.
(38) Wang, T.; Boer-Duchemin, E.; Zhang, Y.; Comtet, G.; Dujardin, G. Excitation of propagating surface plasmons with a scanning tunnelling microscope. *Nanotechnology* **2011**, *22*, 175201.
(39) Wang, T.; Boer-Duchemin, E.; Comtet, G.; Le Moal, E.; Dujardin, G.; Drezet, A.; Huant, S. Plasmon scattering from holes: from single hole scattering to Young's experiment. *Nanotechnology* **2014**, *25*, 125202.
(40) Bharadwaj, P.; Bouhelier, A.; Novotny, L. Electrical Excitation of Surface Plasmons. *Phys. Rev. Lett.* **2011**, *106*, 226802.
(41) Myrach, P.; Nilius, N.; Freund, H.-J. Photon mapping of individual Ag particles on MgO/Mo(001). *Phys. Rev. B: Condens. Matter Mater. Phys.* **2011**, *83*, 035416.
(42) Yu, A.; Li, S.; Czap, G.; Ho, W. Tunneling-Electron-Induced Light Emission from Single Gold Nanoclusters. *Nano Lett.* **2016**, *16*, 5433−5436.
(43) Kuhnke, K.; Große, C.; Merino, P.; Kern, K. Atomic-Scale Imaging and Spectroscopy of Electroluminescence at Molecular Interfaces. *Chem. Rev.* **2017**, *117*, 5174−5222.
(44) Leon, C. C.; Rosławska, A.; Grewal, A.; Gunnarsson, O.; Kuhnke, K.; Kern, K. Photon superbunching from a generic tunnel junction. *Science Advances* **2019**, *5*, eaav4986.
(45) Martín-Jiménez, A.; Fernández-Domínguez, A. I.; Lauwaet, K.; Granados, D.; Miranda, R.; García-Vidal, F. J.; Otero, R. Unveiling the radiative local density of optical states of a plasmonic nanocavity by STM. *Nat. Commun.* **2020**, *11*, 1021.
(46) Le Moal, E.; Marguet, S.; Rogez, B.; Mukherjee, S.; Dos Santos, P.; Boer-Duchemin, E.; Comtet, G.; Dujardin, G. An electrically excited nanoscale light source with active angular control of the emitted light. *Nano Lett.* **2013**, *13*, 4198−205.
(47) Cao, S. Y.; Le Moal, E.; Jiang, Q. B.; Drezet, A.; Huant, S.; Hugonin, J. P.; Dujardin, G.; Boer-Duchemin, E. Directional light beams by design from electrically driven elliptical slit antennas. *Beilstein J. Nanotechnol.* **2018**, *9*, 2361−2371.

https://dx.doi.org/10.1021/acsphotonics.0c00264
ACS Photonics 2020, 7, 1280−1289

(48) Kern, J.; Kullock, R.; Prangsma, J.; Emmerling, M.; Kamp, M.; Hecht, B. Electrically driven optical antennas. *Nat. Photonics* **2015**, *9*, 582.
(49) Du, W.; Wang, T.; Chu, H.-S.; Nijhuis, C. A. Highly efficient on-chip direct electronic-plasmonic transducers. *Nat. Photonics* **2017**, *11*, 623.
(50) Gurunarayanan, S. P.; Verellen, N.; Zharinov, V. S.; Shirley, F. J.; Moshchalkov, V. V.; Heyns, M.; Van de Vondel, J.; Radu, I. P.; Van Dorpe, P. Electrically Driven Unidirectional Optical Nanoantennas. *Nano Lett.* **2017**, *17*, 7433−7439.
(51) Qian, H.; Hsu, S.-W.; Gurunatha, K.; Riley, C. T.; Zhao, J.; Lu, D.; Tao, A. R.; Liu, Z. Efficient light generation from enhanced inelastic electron tunnelling. *Nat. Photonics* **2018**, *12*, 485.
(52) Parzefall, M.; Novotny, L. Optical antennas driven by quantum tunneling: a key issues review. *Rep. Prog. Phys.* **2019**, *82*, 112401.
(53) Zhang, C.; Hugonin, J.-P.; Coutrot, A.-L.; Sauvan, C.; Marquier, F.; Greffet, J.-J. Antenna surface plasmon emission by inelastic tunneling. *Nat. Commun.* **2019**, *10*, 4949.
(54) Johansson, P. Light emission from a scanning tunneling microscope: Fully retarded calculation. *Phys. Rev. B: Condens. Matter Mater. Phys.* **1998**, *58*, 10823−10834.
(55) Uehara, Y.; Kimura, Y.; Ushioda, S.; Takeuchi, K. Theory of Visible-light Emission From Scanning Tunneling Microscope. *Japanese Journal of Applied Physics Part 1-regular Papers Short Notes & Review Papers* **1992**, *31*, 2465−2469.
(56) Aizpurua, J.; Apell, S. P.; Berndt, R. Role of tip shape in light emission from the scanning tunneling microscope. *Phys. Rev. B: Condens. Matter Mater. Phys.* **2000**, *62*, 2065−2073.
(57) Lambe, J.; McCarthy, S. L. Light Emission from Inelastic Electron Tunneling. *Phys. Rev. Lett.* **1976**, *37*, 923−925.
(58) Le Moal, E.; Marguet, S.; Canneson, D.; Rogez, B.; Boer-Duchemin, E.; Dujardin, G.; Teperik, T. V.; Marinica, D.-C.; Borisov, A. G. Engineering the emission of light from a scanning tunneling microscope using the plasmonic modes of a nanoparticle. *Phys. Rev. B: Condens. Matter Mater. Phys.* **2016**, *93*, 035418.
(59) Mitra, J.; Feng, L.; Boyle, M. G.; Dawson, P. Electromagnetic interaction between a metallic nanoparticle and surface in tunnelling proximity—modelling and experiment. *J. Phys. D: Appl. Phys.* **2009**, *42*, 215101.
(60) Rakić, A. D.; Djurišić, A. B.; Elazar, J. M.; Majewski, M. L. Optical properties of metallic films for vertical-cavity optoelectronic devices. *Appl. Opt.* **1998**, *37*, 5271−5283.
(61) Schmidt, F.-P.; Ditlbacher, H.; Hohenester, U.; Hohenau, A.; Hofer, F.; Krenn, J. R. Universal dispersion of surface plasmons in flat nanostructures. *Nat. Commun.* **2014**, *5*, 3604.
(62) Campos, A.; Arbouet, A.; Martin, J.; Gérard, D.; Proust, J.; Plain, J.; Kociak, M. Plasmonic Breathing and Edge Modes in Aluminum Nanotriangles. *ACS Photonics* **2017**, *4*, 1257−1263.
(63) Keast, V. J.; Walhout, C.; Pedersen, T. B.; Shahcheraghi, N.; Cortie, M. B.; Mitchell, D. R. G. Higher Order Plasmonic Modes Excited in Ag Triangular Nanoplates by an Electron Beam. *Plasmonics* **2016**, *11*, 1081−1086.
(64) Schmidt, F.-P.; Ditlbacher, H.; Hohenester, U.; Hohenau, A.; Hofer, F.; Krenn, J. R. Dark Plasmonic Breathing Modes in Silver Nanodisks. *Nano Lett.* **2012**, *12*, 5780−5783.
(65) Krug, M. K.; Reisecker, M.; Hohenau, A.; Ditlbacher, H.; Truegler, A.; Hohenester, U.; Krenn, J. R. Probing plasmonic breathing modes optically. *Appl. Phys. Lett.* **2014**, *105*, 171103.
(66) Schmidt, F.-P.; Losquin, A.; Hofer, F.; Hohenau, A.; Krenn, J. R.; Kociak, M. How Dark Are Radial Breathing Modes in Plasmonic Nanodisks? *ACS Photonics* **2018**, *5*, 861−866.
(67) Bicket, I. C.; Bellido, E. P.; McRae, D. M.; Lagugne-Labarthet, F.; Botton, G. A. Carving Plasmon Modes in Silver Sierpinski Fractals. *ACS Photonics* **2019**, *6*, 2974−2984.
(68) Novotny, L.; van Hulst, N. Antennas for light. *Nat. Photonics* **2011**, *5*, 83−90.
(69) Giannini, V.; Fernandez-Dominguez, A. I.; Heck, S. C.; Maier, S. A. Plasmonic Nanoantennas: Fundamentals and Their Use in Controlling the Radiative Properties of Nanoemitters. *Chem. Rev.* **2011**, *111*, 3888−3912.
(70) Biagioni, P.; Huang, J.-S.; Hecht, B. Nanoantennas for visible and infrared radiation. *Rep. Prog. Phys.* **2012**, *75*, 024402.
(71) Koenderink, A. F. Single-Photon Nanoantennas. *ACS Photonics* **2017**, *4*, 710−722.
(72) Kleinman, S. L.; Frontiera, R. R.; Henry, A.-I.; Dieringer, J. A.; Van Duyne, R. P. Creating, characterizing, and controlling chemistry with SERS hot spots. *Phys. Chem. Chem. Phys.* **2013**, *15*, 21−36.
(73) Zhang, R.; Zhang, Y.; Dong, Z. C.; Jiang, S.; Zhang, C.; Chen, L. G.; Zhang, L.; Liao, Y.; Aizpurua, J.; Luo, Y.; Yang, J. L.; Hou, J. G. Chemical mapping of a single molecule by plasmon-enhanced Raman scattering. *Nature* **2013**, *498*, 82−86.
(74) Lee, J.; Crampton, K. T.; Tallarida, N.; Apkarian, V. A. Visualizing vibrational normal modes of a single molecule with atomically confined light. *Nature* **2019**, *568*, 78−82.
(75) Dong, Z. C.; Zhang, X. L.; Gao, H. Y.; Luo, Y.; Zhang, C.; Chen, L. G.; Zhang, R.; Tao, X.; Zhang, Y.; Yang, J. L.; Hou, J. G. Generation of molecular hot electroluminescence by resonant nanocavity plasmons. *Nat. Photonics* **2010**, *4*, 50−54.
(76) Doppagne, B.; Neuman, T.; Soria-Martinez, R.; López, L. E. P.; Bulou, H.; Romeo, M.; Berciaud, S.; Scheurer, F.; Aizpurua, J.; Schull, G. Single-molecule tautomerization tracking through space- and time-resolved fluorescence spectroscopy. *Nat. Nanotechnol.* **2020**, *15*, 207−211.
(77) Törma, P.; Barnes, W. L. Strong coupling between surface plasmon polaritons and emitters: a review. *Rep. Prog. Phys.* **2015**, *78*, 013901.
(78) Young, K. L.; Jones, M. R.; Zhang, J.; Macfarlane, R. J.; Esquivel-Sirvent, R.; Nap, R. J.; Wu, J.; Schatz, G. C.; Lee, B.; Mirkin, C. A. Assembly of reconfigurable one-dimensional colloidal superlattices due to a synergy of fundamental nanoscale forces. *Proc. Natl. Acad. Sci. U. S. A.* **2012**, *109*, 2240−2245.
(79) Straney, P. J.; Marbella, L. E.; Andolina, C. M.; Nuhfer, N. T.; Millstone, J. E. Decoupling Mechanisms of Platinum Deposition on Colloidal Gold Nanoparticle Substrates. *J. Am. Chem. Soc.* **2014**, *136*, 7873−7876.
(80) Rogez, B.; Cao, S.; Dujardin, G.; Comtet, G.; Le Moal, E.; Mayne, A.; Boer-Duchemin, E. The mechanism of light emission from a scanning tunnelling microscope operating in air. *Nanotechnology* **2016**, *27*, 465201.
(81) HyperSpy 1.0. http://hyperspy.org/hyperspy-doc/v1.0/user_guide/what_is_new.html#v1-0, DOI: 10.5281/zenodo.57882.
(82) COMSOL Multyphisics v. 5.2, AB, Stockholm, Sweden. www.comsol.com.
(83) Persson, B. N. J.; Baratoff, A. Theory of Photon-emission In Electron-tunneling To Metallic Particles. *Phys. Rev. Lett.* **1992**, *68*, 3224−3227.
(84) Chen, S.; Autore, M.; Li, J.; Li, P.; Alonso-Gonzalez, P.; Yang, Z.; Martin-Moreno, L.; Hillenbrand, R.; Nikitin, A. Y. Acoustic Graphene Plasmon Nanoresonators for Field-Enhanced Infrared Molecular Spectroscopy. *ACS Photonics* **2017**, *4*, 3089−3097.
(85) Johnson, P. B.; Christy, R. W. Optical Constants of the Noble Metals. *Phys. Rev. B* **1972**, *6*, 4370−4379.

https://dx.doi.org/10.1021/acsphotonics.0c00264
ACS Photonics 2020, 7, 1280−1289